ACS APPLIED MATERIALS & INTERFACES

www.acsami.org Research Article

Exploring the Chemical Doping of a Water-Soluble Cylindrical Micelle-Forming Conjugated Polyelectrolyte

Xinyu Liu,[#] Alexander F. Simafranca,[#] Julia Chang, Diego Garcia Vidales, Kara Lo, Yutong Wu, Benjamin J. Schwartz,* Yves Rubin,* and Sarah H. Tolbert*

Cite This: ACS Appl. Mater. Interfaces 2026, 18, 11795−11808 Read Online

ACCESS | Metrics & More | Article Recommendations | Supporting Information

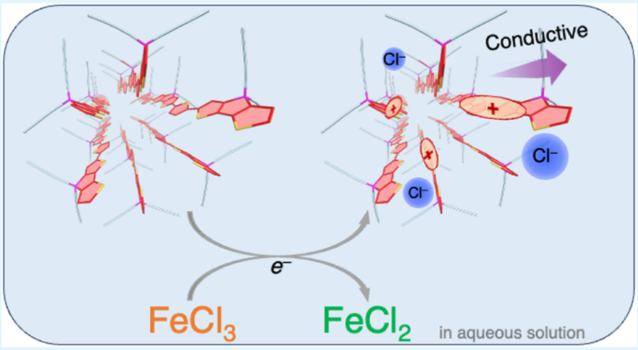

ABSTRACT: The chemical doping of water-soluble conjugated polyelectrolytes (CPEs) offers a promising pathway for the direct printing of semiconducting polymer films by using environmentally friendly solvents. In this study, we explored the chemical doping of the cationic cylindrical micelle-forming CPE poly(cyclopentadithiophene-*alt*-thiophene) (PCT-NBr) in aqueous solution using two Fe(III)-halide dopants, $FeCl_3$ and $FeBr_3$. Treatment with nonoxidizing salts (KCl and KBr) showed that polymer micelles preferentially interact with Br^- ions over Cl^- ions, resulting in a more rigid micelle and spectroscopic evidence of Br^- ion accumulation around the polymer. Doping with both $FeCl_3$ and $FeBr_3$ was followed using UV-visible-near IR absorption spectroscopy, which indicated that the polymer micelles could be stably doped with both iron compounds. $FeCl_3$ was shown to be a stronger dopant due to differences in the lability of Cl^- and Br^- ligands in water. Compared at similar concentrations, $FeCl_3$ induces higher doping levels, while $FeBr_3$ generates more delocalized charge carriers, as evidenced by spectral shifts in the polaronic bands, likely due to weaker counterion Coulombic trapping. Small-angle X-ray scattering was used to confirm that a micellar structure was preserved at all doping levels of PCT-NBr, but the data also indicate increased structural disorder in doped polymer micelles, likely due to partial loss of the polymer's amphiphilic character and ion−polymer interactions. Films spin-cast directly from $FeBr_3$-doped polymer solutions exhibited a stable conductivity of 1.0 S/cm, demonstrating the viability of using doped micellar CPE solutions as a route to single-step deposition of conductive polymer films.

KEYWORDS: *semiconducting polymer, conjugated polyelectrolyte, chemical doping, cylindrical micelle, self-assembly, small-angle X-ray scattering*

INTRODUCTION

In the rapidly advancing field of organic electronics, semiconducting polymers, a class of polymers capable of electronic conduction upon the introduction of charge carriers, have stood out for their high flexibility and mechanical integrity, which make them uniquely suitable for applications in flexible electronics, such as foldable displays and wearable devices.[1−3] The ability to design these polymers at a molecular level offers advantages for tuning electronic properties and optimizing solution processability for printed electronics.[4−8] Designing water-soluble semiconducting polymers through the addition of charged side chains is a particularly promising path toward greener and cheaper electronics manufacturing methods, such as inkjet or roll-to-roll printing.[9−19] Such semiconducting polymers, which combine conjugated backbones with charged side chains, are called conjugated polyelectrolytes (CPEs).

In our previous work, we investigated two CPEs based on poly(cyclopentadithiophene-*alt*-thiophene) (PCT) and poly(fluorene-*alt*-thiophene) (PFT) backbones with geminal quaternary ammonium bromide side chains ($-N^+Me_2EtBr^-$, −NBr for short, Figure 1a) attached at the sp^3 bridging carbon.[16−19] Charged, hydrophilic side chains, such as −NBr, stabilize the otherwise hydrophobic polymer chains in water by imparting an amphiphilic character that encourages self-aggregation into micelles. Guided by Israelachvili's critical packing parameter (CPP) model, which relates the ratio of the hydrophobic volume to the hydrophilic headgroup volume to predict stable micellar geometries,[20] these polymers were designed with straight backbones and large hydrophilic side-chain volumes to encourage cylindrical micelle formation. PCT-NBr and PFT-NBr were shown by solution-phase small-angle X-ray scattering (SAXS) measurements to preferentially assemble into cylindrical micelles in water.[16−19] The formation

Received: December 10, 2025
Revised: January 17, 2026
Accepted: January 18, 2026
Published: February 9, 2026

ACS Publications

https://doi.org/10.1021/acsami.5c24820
ACS Appl. Mater. Interfaces 2026, 18, 11795−11808

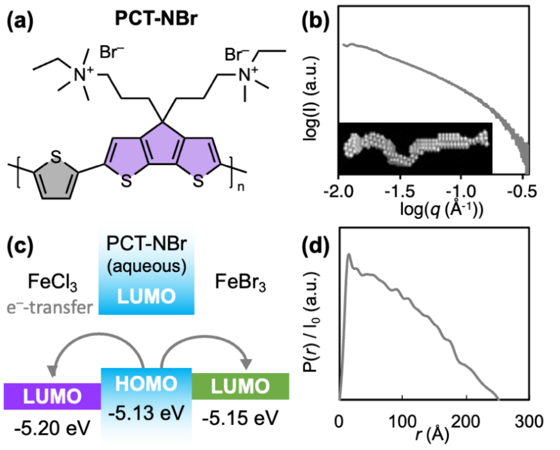

Figure 1. (a) Molecular structure of the PCT-NBr polymer. (b) $I(q)$ trace and (d) pair-distance distribution function (PDDF, $P(r)$) of 1 mg/mL PCT-NBr in aqueous solution. Inset of (b): bead model of the PCT-NBr cylindrical micelle (bead radius is 3.6 Å). (c) Relative electronic energy levels of PCT-NBr, $FeCl_3$, and $FeBr_3$, illustrating that $FeCl_3$ and $FeBr_3$ can dope PCT-NBr by removing electrons from its HOMO in aqueous solution.

of cylindrical micelles aligns the conjugated polymer backbones within micellar cores, thereby reducing defects in conduction pathways and thus enhancing charge transport.[19]

Here, we build on our past work by chemically doping our polymer micelles to create conducting assemblies in solution and observe the effects of micelle formation on charge transport. Because ion-pairing interactions between the charged side chains of a CPE and ions in solution play an important role in stabilizing polymer micelles in solution, disruption of ion pairing can influence both the colloidal stability and the morphology of the resulting assemblies. Several theoretical frameworks describe how specific ions contribute to the overall stability. The Hofmeister series ranks ions on their tendency to disrupt water packing and salt-in macromolecules (chaotropes) or preserve water packing and salt-out macromolecules (kosmotropes). Similarly, Collin's Law of Matching Water Affinities explains this behavior by noting that ions with similar tendencies to bind water (water affinity) are more likely to form ion pairs.[21−25] Strong ion pairing reduces electrostatic repulsion between charged side chains, decreasing the effective size of an amphiphile's polar headgroup and influencing the shape of any micelles that form.[20]

To experimentally probe these structural changes, solution SAXS serves as a powerful tool for determining the micelle size and shape in solution. For colloidal solutions of aggregates with a defined shape, the SAXS data can be modeled to provide a detailed picture of the shape of the aggregates in solution. In this work, SAXS is employed to investigate how ion pairing and counterion identity influence micelle morphology, bridging theoretical predictions with experimental observations in these unique cylindrical micelle-forming CPEs. SAXS also allows us to determine whether micellar structures in solution are preserved upon chemical doping of these semiconducting polymer micelles to form conducting polymer wires.

Although the self-assembly and morphology of CPEs in solution are essential for their solution processability, their electronic properties in the solid state ultimately dictate their functionality in optoelectronic applications. To generate a sufficient density of mobile charge carriers and render these films conductive, doping is required and can be performed either chemically (i.e., with molecular oxidants) or electrochemically (i.e., with voltage).[26−44] Most semiconducting polymers have shallow highest occupied molecular orbital (HOMO) energy levels that favor *p*-type doping, in which electrons are removed from the polymer's valence band, leaving behind mobile, positively charged holes (radical cations) as charge carriers.[26−44] These holes couple with local structural distortions of the polymer backbone to form polarons, and polarons must associate with counter-anions to balance their charge.[27,29] At high doping levels, doubly charged carrier species called bipolarons will form.[30,45−47] Doping progress can be readily tracked by UV-visible-near IR (NIR) absorption spectroscopy through the emergence and growth of intrabandgap optical transitions associated first with polarons (P1—valence band edge to polaronic ground state, and P2—polaronic ground state to excited state), then later with bipolarons (BP1—valence band edge to bipolaron ground state).[47−49]

The fact that the polarons in semiconducting polymers show clearly defined absorption peaks also provides another useful tool for assessing the electronic properties of our doped polymer micelles. Spano and coworkers have used a Holstein-style polaron model to relate polaronic absorption features to charge carrier delocalization in conjugated polymers.[50] Specifically, the position of the P1 absorption peak has been shown to reflect the polaron coherence length, with more delocalized polarons showing redder absorption peaks.[50] Experimentally, these redder P1 peaks have been found to correlate with higher charge carrier mobility.[51,52] This makes the theory a powerful tool for probing carrier delocalization and estimating mobility through optical spectroscopy, both in solution and solid-state thin films.

Most doping of organic-soluble, nonpolyelectrolyte semiconducting polymers is done by sequential chemical doping, in which a polymer film is first cast in undoped form and then infiltrated with a chemical dopant from a swelling solvent.[28,31,32,37−44] Blend doping, where the polymer and the dopant are mixed together in solution, is usually undesirable for these polymers, as the organic solvents used to dissolve the polymers are poor solvents for the doped polymer segments and counterions, resulting in polymer aggregation and precipitation.[31,32] For water-soluble CPEs, however, doping can be performed directly in solution before film deposition, offering intimate mixing between dopants and polymers and eliminating sequential processing steps. Despite these benefits, research on the chemical doping of CPEs in aqueous solutions remains limited. Although Nguyen et al. have studied the acid doping of water-soluble CPEs with random coil structures,[15] to our knowledge, no prior studies exist on the doping of aqueous CPE solutions with chemical oxidants, particularly those that self-assemble into cylindrical micelles.

In this study, we investigate the chemical doping of cylindrical micelle-forming conjugated polyelectrolyte PCT-NBr in aqueous solutions using Fe(III)-halide oxidants ($FeCl_3$ and $FeBr_3$) as dopants. Through a combination of UV-visible-NIR spectroscopy and solution SAXS, we examine how doping affects both the optoelectronic properties and morphology of the polymer micelles. We first treat PCT-NBr micelles with halide salts (KCl and KBr), then with the Fe(III)-halide dopants, to explore how the anions Cl^- and Br^- affect dopant speciation, micellar morphology, doping efficiency, and polaron delocalization. We then explore how these effects translate from solution to the solid state and demonstrate that conductive films can be fabricated by spin-casting directly from predoped aqueous micellar solutions. These findings provide molecular-level insight into the interplay between dopant chemistry, counterion interactions, and polymer assembly, offering design principles for future aqueous-processed electronic materials.

■ RESULTS AND DISCUSSION

Our previous work has demonstrated that the CPE poly(cyclopentadithiophene-*alt*-thiophene) (PCT-NBr, Figure 1a) and related polymers self-assemble into cylindrical micelles in aqueous solutions.[53−55] This can be observed through modeling of solution SAXS scattering profiles ($I(q)$) and calculation of pair-distance distribution functions (PDDF) (Figure 1b and d).[19,56−59] The PDDF profile shows a peak at low r, corresponding to correlations across the micellar radius, and a nearly linear region, corresponding to correlations along the cylinder length (Figure 1d). Some curvature in the linear portion arises from the bent micellar structure in solution. This conclusion was further supported by bead modeling of the raw $I(q)$ data, which is a Monte Carlo method to construct a geometry that will produce the observed scattering profiles. The bead models produce worm-like micelles (inset in Figure 1b), in good agreement with conclusions drawn from PDDF curves. In considering all of the micelle-forming polymers that we have been able to synthesize to date,[16−19] PCT-NBr was selected for use in this doping study both for its well-ordered micellar structure and for its high HOMO level, which should facilitate *p*-type doping.

For dopants, this study employs two Fe(III)-halide dopants, $FeCl_3$ and $FeBr_3$, chosen for their water solubility, low cost, low toxicity, and low environmental risk compared with other metal-centered oxidants. Cyclic voltammetry (CV) measurements show that the HOMO level of PCT-NBr is −5.13 eV, while the LUMO levels of $FeCl_3$ and $FeBr_3$ in aqueous solution are approximately −5.20 eV and −5.15 eV vs vacuum, respectively (Figure 1c and Figure S1, calculated according to literature methods).[60,61] These values indicate that oxidation of PCT-NBr by both dopants should be thermodynamically spontaneous, and both $FeCl_3$ and $FeBr_3$ are therefore compatible chemical oxidants for PCT-NBr micelles.

Effects of Free Anions on PCT-NBr Micellar and Electronic Structure

As a polyelectrolyte, the PCT-NBr polymer can interact with free ions in solution through its quaternary ammonium headgroups, and the solvation of PCT-NBr micelles in water relies on interactions between water and these hydrophilic headgroups. Competing interactions with free ions may disrupt water−polymer interactions and cause morphological changes in the micelle packing. Because Cl^- and Br^- ions are released during the hydrolysis of $FeCl_3$ and $FeBr_3$, their effects on the structure and electronic states of PCT-NBr micelles must first be understood before changes due to polaron formation can be assessed.

To probe how free Cl^- and Br^- ions influence the micellar structure, solution SAXS studies were performed on PCT-NBr micelles in the presence of KCl and KBr salts. Figure 2a and Figure S2 show the PDDF patterns for PCT-NBr micelles in the presence of increasing concentrations of KCl and KBr, with the corresponding $I(q)$ plots in Figure S3. At low salt concentrations (0.3 mM), the PDDF patterns for both salts show a long linear decay region similar to those of salt-free PCT-NBr, which indicates that the micelles are cylindrical in shape. The slightly convex curvature in this linear region indicates some micellar bending, as seen in the bead models (Figure 2b), though the linear Porod slope in the intermediate q region of the sample's $I(q)$ scattering pattern remains fairly close to 1 (Table 1). The small peak at high r values in these samples is indicative of a small amount of micellar clumping that occurs with low probability relative to dispersed cylindrical micelles.

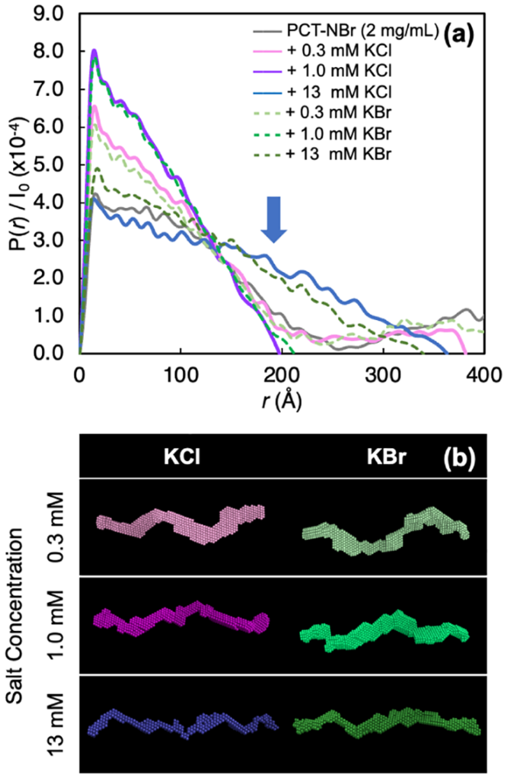

Figure 2. (a) Pair-distance distribution functions (PDDF, $P(r)$) of aqueous 2 mg/mL PCT-NBr solutions containing KCl or KBr at low, medium, or high concentrations. (b) Bead models showing micellar structural changes with increasing salt concentration. Both KCl and KBr show a micellar straightening effect at low to medium salt concentrations, while KCl shows increasing micellar bending at higher salt concentrations (blue arrow). Bead radii (from top to bottom): 1.8 Å, 1.7 Å, 2.6 Å, 1.8 Å, 1.7 Å, 2.9 Å, respectively.

At medium salt concentrations (1.0 mM), the PDDF patterns for both salts exhibit a very linear decay region with little convex curvature and without high-r (aggregation) peaks. Surprisingly, these differences suggest that the polymer micelles are straighter at medium salt concentrations than in salt-free or low-salt PCT-NBr solutions, a conclusion that is confirmed by the bead models (Figure 2b). This behavior is attributed to the screening of the electrostatic repulsions between the quaternary ammonium head groups due to the increased ionic strength, which should allow for closer packing of the polymer side chains, thus stabilizing the micellar assembly.

At high salt concentrations (13 mM), the linear regions of the PDDF patterns for both salts extend to higher correlation

Table 1. Parameters Correlated with Micellar Length and Size Fitted from $I(q)$ Using the Global Guinier−Porod Method for PCT-NBr upon Addition of Various Concentrations of KBr or KCl[a]

	R_{g1} (Å)	R_{g2} (Å)	$S1$	D (Å)	L (Å)
PCT-NBr 2 mg/mL	6.5	60	1.10	18.4	208
KBr 0.34 mM	6.5	56	1.08	18.3	193
KBr 0.74 mM	6.5	54	1.09	18.4	185
KBr 1.01 mM	6.5	53	1.09	18.5	182
KBr 1.34 mM	6.5	52	1.08	18.5	179
KBr 6.71 mM	6.8	59	1.08	19.3	205
KBr 13.4 mM	6.9	74	1.08	19.4	256
KCl 0.34 mM	6.5	55	1.08	18.3	191
KCl 1.01 mM	6.3	52	1.09	17.7	179
KCl 1.34 mM	6.3	50	1.09	17.9	171
KCl 6.71 mM	6.2	60	1.08	17.4	207
KCl 13.4 mM	6.0	74	1.08	16.9	256

[a] R_{g1}: radius of gyration in the low-Q Guinier region; R_{g2}: radius of gyration in the high-Q Guinier region; $S1$: slope of intermediate Porod region; D: diameter of cylindrical micelle; L: length of cylindrical micelle.

lengths, indicating an increase in the micellar persistence length, which agrees with a noticeable increase in the persistence length from global Guinier−Porod fitting parameters (Table 1). Even though the shape of the PDDF patterns for both ions tracks at the low and medium salt concentrations, they diverge slightly in shape at high salt concentration. The PDDF for the KCl-treated sample shows a peak emerging near ~200 Å (where the arrow points in Figure 2a), indicating the onset of long-range micellar bending.

This divergence in ion behavior can be rationalized by Collins' Law of Matching Water Affinities, which states that ion pairing is strongest between ions with similar hydration character. Weakly hydrated quaternary ammonium groups ("chaotropic" in the Hofmeister series) pair more tightly with similarly weakly hydrated Br^- ions than with more strongly hydrated Cl^- ions ("kosmotropic" in the Hofmeister series).[21−25] As Israelachvili proposed in his critical packing parameter (CPP) framework, tighter ion pairing reduces the effective side-chain headgroup size and inter side-chain repulsion.[20,62] In the presence of Cl^- ions, Cl^- can replace the Br^- ions originally associated with the polymer through mass action, but weaker ion pairing between Cl^- ions and headgroups cannot reduce side-chain headgroup repulsion as efficiently, thereby leading to a larger side-chain headgroup size. This leads to a reduction in the number of polymer chains in the micelle, reflected in the slightly reduced micelle diameter, which allows for more flexible micelles that can bend over long length scales.

In addition to structural impacts, free anions have a subtle, yet noticeable effect on the electronic structure of the polymers in the micelle. Specifically, a slight red shift in the bandgap energy occurs in the presence of Br^- ions, whereas minimal shift is observed with Cl^- ions (Figure 3 and Figure S4). Due to the subtlety of the spectral changes, a cross-correlation analysis (see Supporting Information for the details) was employed to more clearly track the red shift. Figure 3a shows the cross-correlation of the bandgap absorbance near its peak between PCT-NBr with and without added salt as a function of energy offset. The auto-correlation (i.e., self-correlation) of the salt-free PCT-NBr polymer is included as a reference. The cross-correlation curves are nearly symmetric near the bandgap peak maximum, and a visible displacement toward lower energy indicates a red shift. Although a clear and progressive red shift is noticeable in the KBr-treated samples, the KCl-treated samples show only a small red shift that does not progress with increasing concentration.

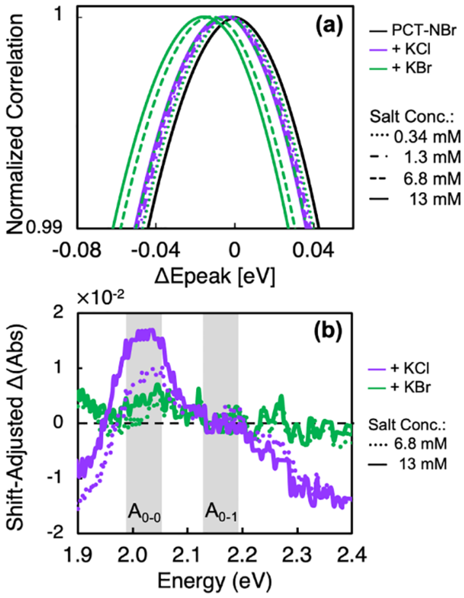

Figure 3. (a) Normalized auto/cross-correlation functions near the bandgap absorbance peak as a function of energy offset. A noticeable red shift is observed in KBr-treated aqueous 2 mg/mL PCT-NBr solutions. (b) Red-shift-corrected difference in absorbance between untreated and salt-treated aqueous PCT-NBr solutions.

The red shift observed in KBr-treated PCT-NBr can be linked to two phenomena, the first of which is counterion condensation in polyelectrolytes.[63−74] Because of the compatible water affinities of the quaternary ammonium headgroups and Br^- ions, Br^- ions will preferentially condense around the micelles.[25,63,64] This increases the local ion density and has a stabilizing electrostatic effect on the polar exciton state, leading to a red shift of the bandgap energy. The second effect comes from the fact that micelles are straighter in the presence of KBr; this may also allow for greater exciton delocalization and thus a red-shifted bandgap absorption.

Using the red shifts extracted from Figure 3a, red-shift-corrected differences in absorbance between salt-treated and untreated PCT-NBr solutions can be calculated (Figure 3b). At medium and high salt concentrations, an A_{0-0} vibronic enhancement is seen in KCl-treated samples that does not occur with the added KBr. This increase in A_{0-0} intensity indicates an enhancement of head-to-tail (J-type) excitonic dipole coupling.[65−68] Previous studies have demonstrated that, in the presence of weak H-type interchain coupling, a straight semiconducting polymer chain will show predominantly J-type coupling.[65−68] The observed enhancement of J-type or a reduction in H-type character coincides with the reduction in the micelle diameter and the increase in micelle bending due to a potential reduction in the number of polymer chains per micelle. All of these changes occur because of the higher headgroup repulsion in the presence of Cl^-, which wedges adjacent chains apart within a micelle. Together with the SAXS data, ion exchange of the polymer's Br^- ions for Cl^- ions is

https://doi.org/10.1021/acsami.5c24820
ACS Appl. Mater. Interfaces 2026, 18, 11795−11808

therefore shown to tune the micelle rigidity and the polymer electronic structure in predictable and understandable ways.

Doping of PCT-NBr Aqueous Solutions with Fe(III) Halides

We now turn to the doping of PCT-NBr micelles with Fe(III)-halide dopants in water, beginning with $FeCl_3$. UV-visible-NIR spectroscopy is an easy way to monitor the progression of doping due to the appearance of intrabandgap states arising from the polaron dopant bands (Figure 4a). Because PCT-NBr has a high molar absorptivity ($\varepsilon = 3.8 \times 10^4$ $(M{\cdot}cm)^{-1}$, Figure S5) and water absorbs strongly in the infrared region, a custom short-path-length (~60 μm) solution cell with sapphire windows was used for optical measurements (Figure 4b).

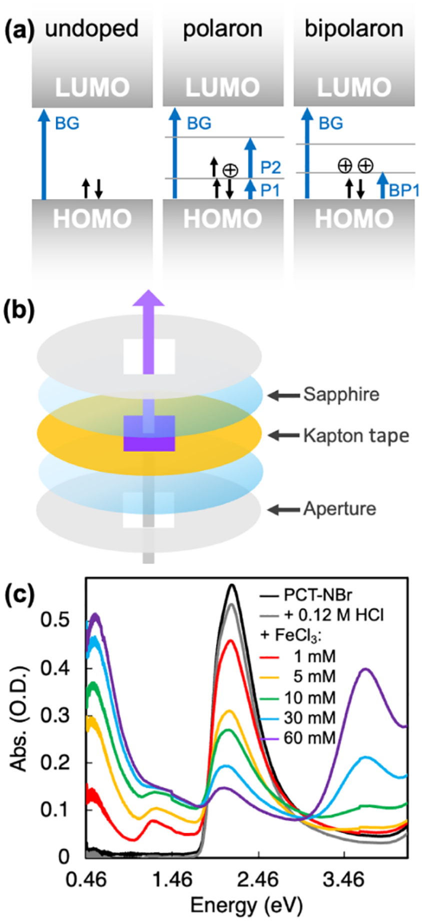

Figure 4. (a) Schematic electronic structure of an undoped semiconducting polymer, a polaron, and a bipolaron. (b) Schematic of a sapphire-windowed ultrathin spectroscopic solution cell. (c) UV-visible-near IR spectra of aqueous solutions of 2 mg/mL PCT-NBr doped with $FeCl_3$ (HCl-stabilized).

The UV-visible-NIR absorption spectra of $FeCl_3$-doped PCT-NBr solutions can be used to quantify the extent of doping with increasing $FeCl_3$ concentration (Figure 4c). Because Fe(III) salts readily hydrolyze in neutral or basic water to form oxide precipitates that reduce the concentration of redox-active species,[69−75] solutions of the $FeCl_3$ dopant were stabilized with HCl. The HCl concentration was chosen so that the dominant solution-phase species was $FeCl_2(H_2O)_4^+$, as determined by solution-phase conductivity measurements, measured as a function of the HCl concentration (Figure S6). PCT-NBr treated with HCl alone shows no evidence of the P1 or P2 transitions that would indicate polaron formation (gray line), indicating acid alone does not dope PCT-NBr. As the $FeCl_3$ concentration increases, the emergence of P1 (~0.5 eV) and P2 (~1.2 eV) polaron absorption peaks and the simultaneous decrease in the intensity of the bandgap transition centered at ~2.2 eV indicate increasing polaron formation. At concentrations above 10 mM, the P1 peak blue shifts, and the dip at 0.9 eV starts to disappear. Both changes can be assigned to the ingrowth of a bipolaron BP1 transition, which is generally centered between 0.8 and 1 eV.[30,45−47]

Any positively charged polarons or bipolarons that form during doping must be charge-balanced by counter-anions in solution. When $FeCl_3$ is used to dope semiconducting polymers in organic solvents, $FeCl_4^-$ typically serves as the counter-anion.[76,77] However, anionic Fe(III) and Fe(II) species like $Fe(III)Cl_4(H_2O)_2^-$ and $Fe(II)Cl_4(H_2O)_2^{2-}$ are only a small fraction of the total ionic species in water at the concentrations of $FeCl_3$ used for doping.[70−75,78,79] Indeed, in Figure 4c, there is an absorbance peak centered at ~3.7 eV that grows significantly with increasing $FeCl_3$ concentration. This peak is associated with $FeCl_2(H_2O)_4^+$ complexes,[78,79] indicating that the major Fe(III) species in water are indeed cationic. It is therefore likely that the plentiful Cl^- ions in solution serve as the counter-anions for the newly formed polarons.

As additional evidence, colorimetric analysis was performed on the ultrafiltrate collected from $FeCl_3$-doped PCT-NBr samples using bipyridyl (bipy) complexation to produce the color change (Figures S7 and S8). If the counterion to the polaron was an Fe-containing ion, there should be an observable loss of Fe in the ultrafiltrate due to the association of Fe with the doped polymer sample. In the assay, both Fe(II) and Fe(III) species were quantified, and across all samples, Fe loss potentially attributable to polymer association was found to be less than ±5% and did not vary in a monotonic fashion (Table 2), indicating that all iron species remain primarily as free ions in solution during doping. This finding further supports the idea of Cl^- ions as counter-anions in aqueous $FeCl_3$ doping.

Table 2. Colorimetric Characterization of Fe-Content in $FeCl_3$-doped PCT-NBr Solutions

Input [Fe] (mM)	Recovered [Fe] (mM)	Difference in [Fe] (%)	$[Fe^{2+}]$ (mM)	$[Fe^{2+}]$/ [Fe] (%)
0.5	0.5	+0	0.12 ± 0.02	24 ± 4
1	1.0	+0	0.13 ± 0.01	13 ± 1
5	5.2	+4	0.24 ± 0.02	5.2 ± 0.6
10	9.5	−5	0.27 ± 0.01	2.8 ± 0.4
30	29.0	−3	0.33 ± 0.04	1.0 ± 0.2

The ratio of Fe(II) detected in the filtrate to total Fe detected is the Fe conversion ratio, a measure of the dopant efficiency. A high dopant efficiency indicates that most of the input dopant molecules result in the formation of charge carriers. The highest observed conversion ratio was 24% at 0.5 mM $FeCl_3$. The conversion ratio decreases with increasing $FeCl_3$ concentration, as expected for a reaction with a low driving force for electron transfer from PCT-NBr to $FeCl_3$ (~70 meV).

Having established the doping behavior of PCT-NBr with $FeCl_3$, we next sought to explore how the halide ion of Fe(III)-halide complexes influences the dopant efficiency and polymer−dopant interactions. $FeBr_3$ offers a useful comparison

https://doi.org/10.1021/acsami.5c24820
ACS Appl. Mater. Interfaces 2026, 18, 11795−11808

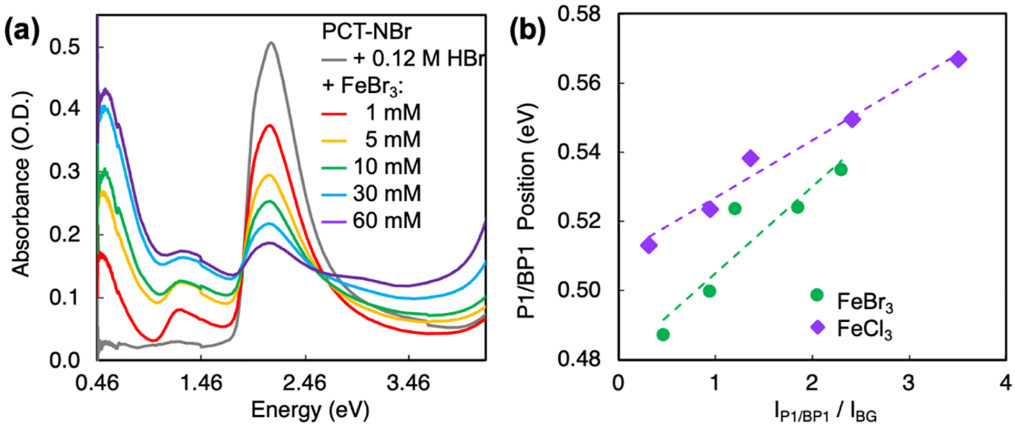

Figure 5. (a) UV-visible-NIR spectra of aqueous solutions of 2 mg/mL PCT-NBr doped with $FeBr_3$ (HBr-stabilized). (b) Red shift of the P1/BP1 absorbance peak position in $FeBr_3$-doped PCT-NBr with doping level quantified by the P1/BP1-to-bandgap intensity ratio.

due to its similar redox chemistry but a larger, more polarizable halide ion. Comparing these two dopants provides insights into how dopant speciation and counterion effects influence the structure and properties of doped CPEs in aqueous environments.

As with $FeCl_3$, an understanding of the speciation of $FeBr_3$ in water is useful to interpret the dopant behavior. UV-visible-NIR spectroscopy again proved useful toward this goal; we observe the red edge of an absorbance peak centered near ∼5.1 eV is in HBr-stabilized, $FeBr_3$-doped samples of PCT-NBr (Figure 5a), which is different from the $FeCl_2(H_2O)_4^+$ peak observed near ∼3.7 eV in $FeCl_3$-doped samples (Figure 4c). This bluer Fe peak is associated with the $Fe(H_2O)_6^{3+}$ complex.[78] Thus, in contrast to $FeCl_3$, which retains some chloride ligands in water, the Br^- ligands in $FeBr_3$ are largely replaced by H_2O molecules. This exchange behavior is consistent with the ranking of these halide ions on the spectrochemical series, where Br^- is a weaker-field ligand than Cl^- and is therefore more easily displaced by water.

Comparing the UV-visible-NIR spectra for the two dopants, the $FeCl_3$-doped samples show more doping than the $FeBr_3$-doped samples at the same dopant concentration. The P1 absorbance peak (∼0.5 eV) at a given dopant concentration is higher in intensity with $FeCl_3$ than with $FeBr_3$, and the bandgap absorbance peaks are more bleached (Figures 4c, 5a, and S13c), indicating $FeCl_3$ has a higher dopant efficiency. This is also consistent with the more electron-withdrawing nature of Cl^- ligands and their lower tendency to be exchanged by water, both of which contribute to the stronger oxidizing potential of the Fe(III) center. These findings highlight the importance of considering possible ligand exchange with water and ion speciation when using metal-centered oxidants as dopants for CPEs in water.

Knowing that free halide ions are the counter-anions for polarons formed when the PCT-NBr micelles are doped, we next consider how the halide identity may affect the nature of the polaron. At similar doping levels (quantified by the ratio of the combined intensities of the P1 polaron and BP1 bipolaron peaks to the bandgap peak intensity, $I_{P1/BP1}$ /I_{BG}), the P1/BP1 peak position for $FeBr_3$-doped PCT-NBr is red shifted relative to $FeCl_3$-doped samples (Figure 5b), an effect that is most dramatic at lower doping levels, where the peak shows pure P1 character with no overlapping BP1 absorbance. Based on a broad range of theoretical and experimental studies, redder P1 peaks are indicative of more delocalized polarons that are less Coulombically bound with their counterions.[28,50−52] The formation of more delocalized polarons with $FeBr_3$ doping is consistent with the larger, more polarizable Br^- counter-anions compared to smaller, less polarizable Cl^- counter-anions.[80,81] Br^- counter-anions therefore facilitate greater polaron delocalization and could potentially produce polarons with higher mobility.

Effects of Doping on Polymer Micellar Structure

The optical responses observed in doped PCT-NBr raise questions about its underlying structural morphology: do the micellar assemblies observed in the neutral state persist upon doping? Since introducing a positive charge onto the polymer backbone increases its hydrophilicity and reduces its amphiphilic character, doping could potentially alter its geometry or disrupt micelle formation. Using the structure of PCT-NBr micelles in the presence of salts as a baseline, we sought to isolate the structural impacts of polaron formation within the micelles during doping. To investigate this, changes in the shape of doped polymer micelles were observed by solution SAXS measurements. Although both $FeCl_3$ and $FeBr_3$ are effective aqueous oxidants, our structural analysis focused on $FeCl_3$-doped PCT-NBr, as the high electron density of the Br atom and the propensity for $FeBr_3$ to react under X-ray irradiation both make $FeBr_3$-doped samples incompatible with the SAXS X-ray beam setup.

Separate from the effects of polaron formation, the presence of acid (HCl in the case of $FeCl_3$) for dopant stabilization could influence the micellar structure. Indeed, the addition of HCl to PCT-NBr micelles alone led to an abrupt increase in scattering intensity around ∼100 Å, indicating significant bending of the cylindrical structures (Figure 6a).[19] Relative to the position of the bending peak observed with KCl at ∼200 Å, the shift in the position of the bending peak to a lower correlation distance of ∼100 Å with HCl reflects an increase in the average curvature of the bent segments. Under low-pH conditions, increased hydration of the quaternary ammonium side chains should reduce counterion binding and increase electrostatic repulsion,[20] effectively increasing the headgroup volume and leading to overcrowding within the micelle corona. These effects should both directly promote micelle bending and disorder and should facilitate a reduction in the number of polymer chains per micelle, a process that would also allow for additional micelle flexibility. The effects of acid on PCT-NBr

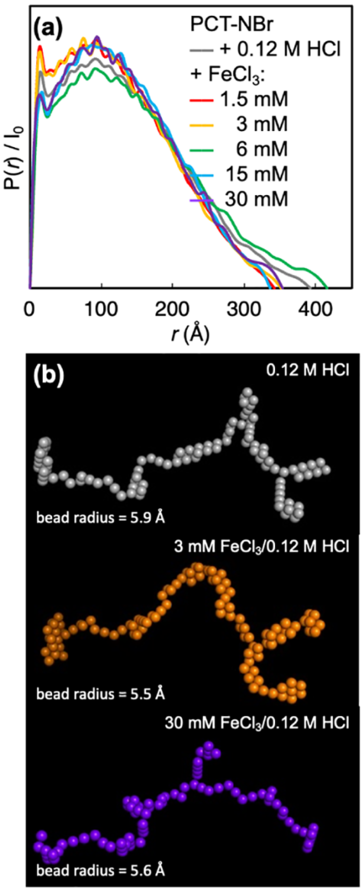

Figure 6. (a) PDDF of $FeCl_3$-doped aqueous 2 mg/mL PCT-NBr solutions. (b) Bead models of $FeCl_3$-doped aqueous PCT-NBr solutions. More $I(q)$ data and bead models are found in Figures S9–S11.

micelles are pronounced and cannot be neglected in analyzing structural changes during doping.

With the addition of the dopant $FeCl_3$, additional changes in the polymer micelle structures are observed (Figure 6 and Table S1). Although structurally similar to HCl-treated PCT-NBr at low $FeCl_3$ concentrations, higher concentrations of $FeCl_3$ increase the intensity of the micellar bending peak relative to the cylindrical portion of the PDDF. This is notably the opposite behavior of what is typically observed in semiconducting polymers upon doping. For nonpolyelectrolyte semiconducting polymers in the solid state, polaron formation is typically associated with straightening of the polymer chains because of polaron delocalization along the polymer backbone.[82−85] In contrast, polarons here have a clear disordering effect on the PCT-NBr micelles. The mechanism for this increase in disorder is believed to be a loss of the hydrophobic character of the backbone due to the formation of positively charged polarons. These polaron charges cause repulsion between the polymer backbone and the positively charged side chains, disrupting the amphiphilicity of the polymer chains that allows them to form ordered micelles. The combined influence of elevated Cl^- ion concentration, stronger hydration due to the lowered pH, and the loss of hydrophobic character of the backbone contributes to the disruption of a clean cylindrical micelle morphology in $FeCl_3$-doped PCT-NBr samples.

Despite the deviations from an ideal cylindrical morphology, the bead models for HCl-treated and $FeCl_3$-doped PCT-NBr in Figure 6b indicate that the polymers fundamentally retain their cylindrical morphology, albeit with significant disorder. The SAXS data also show a thinning of the polymer micelle at the highest doping levels, as indicated by the shift in the first PDDF peak to smaller size (Figure 6a) and the decreased thickness of the worm-like chain in the bead models (Figure 6b). However, it is worth noting that although solution-phase SAXS reveals increased nanometer-scale micelle bending and disordering upon the addition of acid or dopant, the local structure of the polymer chains within the micelle cores remains largely unaffected, as evidenced by the unchanged position of the main bandgap absorption and the vibronic subfeatures, as shown in Figures 4, 5, and S12.

Interestingly, the bead model data also opens up the interesting possibility of micellar branching at the highest $FeCl_3$ concentrations. In such structures, correlations between branches contribute to the micellar bending peak, while the branches themselves maintain cylindrical scattering features. We have previously observed that similar, but more disordered, CPEs can form gels at high polymer concentrations due to entanglement or branching between polymer micelles.[16,17] In the case presented here, branching induced by doping and acid effects may similarly increase micellar entanglement and network formation. This behavior warrants future study in solid-state thin films, as the formation of branched micelles could prove advantageous for the deposition of polymer films with multidimensional percolation pathways for electronic conduction.

Spin-Cast Films of Doped PCT-NBr Solutions

Unlike organic-soluble semiconducting polymers that require post-deposition sequential doping,[31,32,37−44] doped CPE films can be spin-cast directly from iron-halide-containing aqueous solutions. This approach eliminates film post-processing steps and provides a platform for studying how doping behavior evolves during the transition from solution to the solid state. Based on UV-visible-NIR absorption spectra, PCT-NBr films doped with $FeCl_3$ and $FeBr_3$ both showed a sudden increase in the P1/BP1-to-bandgap peak absorbance intensity ratio ($I_{P1/BP1}/I_{BG}$) above 62.5 mM of Fe(III) (Figures 7, S13 and Table S2). This abrupt increase in dopant efficiency can be attributed to an increase in halide coordination in the Fe(III) complexes as the local halide concentration increases during film drying. This conclusion is supported by the fact that the Fe(III) peak shifts from ~3.7 eV, corresponding to $FeCl_2(H_2O)_4{}^+$, to ~3.4 eV and ~4.0 eV for $FeCl_3(H_2O)_3$ in Figure 7a, and from ~5.1 eV for $Fe(H_2O)_6{}^{3+}$ to ~2.6 eV and ~3.1 eV for $FeBr_3(H_2O)_3$ in Figure 7b,[78,79] thereby increasing the oxidizing power and effectiveness of the Fe(III) species in solution. The increased absorption in the visible region for films doped with $FeBr_3$ at the highest doping levels is attributed to the low-energy tail of the 2.6 eV $FeBr_3(H_2O)_3$ absorption, which extends into the redder region beyond the polymer peak maximum, combined with increased scattering from the extra salt present in the films. The higher solubility of $FeBr_3$ in comparison to $FeCl_3$ is expected to favor the formation of larger salt crystals during film drying, thereby producing more scattering.[86,87] In addition to the dramatic increase in the P1/BP1-to-bandgap peak absorbance intensity ratio at higher doping levels, both $FeCl_3$- and $FeBr_3$-doped samples show a shift in the P1 band maximum to higher energy, likely due to the formation of an overlapping bipolaron

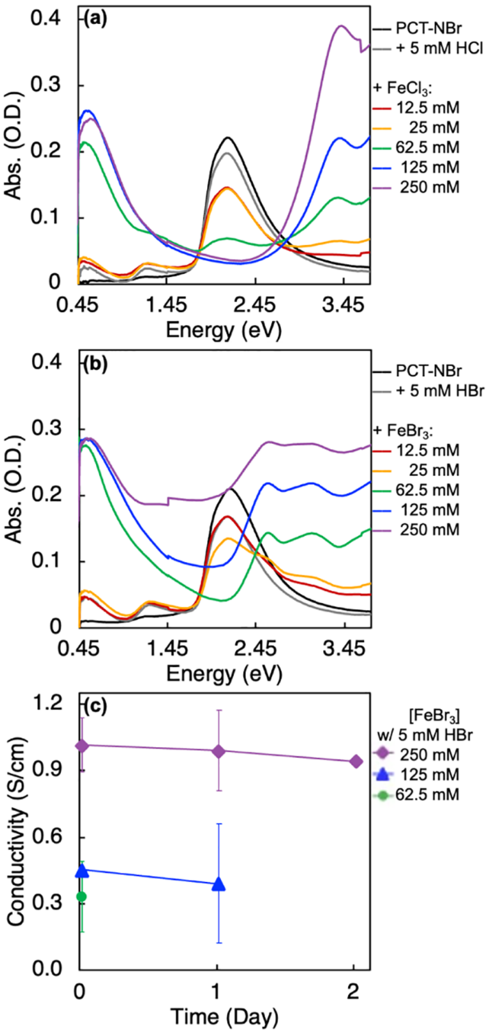

Figure 7. UV-visible-NIR absorbance spectra of films deposited from (a) $FeCl_3$-doped aqueous solutions (HCl-stabilized) and (b) $FeBr_3$-doped aqueous solutions (HBr-stabilized). Excess dopant retained in the films, particularly in $FeBr_3$-doped samples, causes light scattering, leading to elevated intensity in the bandgap region of the absorption spectra. (c) Conductivity of $FeBr_3$-doped PCT-NBr films and changes in that conductivity after storage in air for up to 2 days.

absorption peak, which generally appears around 1 eV and is expected at higher doping levels.[30,45−47]

To investigate how counterion effects observed in solution translate to electronic performance in the solid state, conductivities were measured for the $FeCl_3$- and $FeBr_3$-doped films. Although the $FeCl_3$-doped films did not exhibit measurable conductivity at any dopant concentration, films doped with 250 mM $FeBr_3$ showed a conductivity of 1.0 S/cm. Importantly, the films retained 92% of that conductivity value after 2 days stored under ambient conditions (Figure 7c and Table S3). Films doped with less $FeBr_3$ showed lower conductivity but similar stability in air (Figure 7c and Table S3). The fact that the $FeBr_3$-doped films display higher conductivity than the $FeCl_3$-doped films agrees with the more delocalized polarons observed spectroscopically due to the weaker Coulombic binding of polarons with Br^- ions compared to Cl^- ions. Additionally, the retention of film conductivity after storage under ambient conditions with oxygen and humidity highlights the advantages of water-processed conductive films with a self-assembled architecture that isolates the conductive polymer backbones from polar side chains or counterions.

Although conductivity is a practically useful figure of merit, the more fundamental value is carrier mobility. This is usually measured using the Hall effect to determine the carrier density, which is combined with the conductivity to calculate the mobility. Unfortunately, determining carrier density in films with a high density of ionic species via the Hall effect is challenging due to the screening of the Hall voltage by mobile ions, an effect that results in unreliably low carrier densities and thus artificially high carrier mobilities (Table S4).[88−90] Instead, we employed an optical calibration method based on the oscillator-strength-weighted area of the P1 absorption band, calibrated using poly(3-hexylthiophene) (P3HT), to estimate charge carrier density and thus carrier mobility.[52,91,92] The details of the measurement and the resulting carrier mobility estimates are found in Figures S14,S15 and Tables S4,S5.

One question related to these electrical studies is whether the polymers retain their micellar structure in the solid state. Although SAXS is an ideal way to examine polymer morphology in solution, we turned to atomic force microscopy (AFM) to study the morphology of both undoped and doped films. Samples were prepared by drop-casting aqueous solutions containing 50 μg/mL PCT-NBr plus any acid or Fe(III) salts needed for doping onto freshly cleaved mica; 10% (v/v) MeOH was also added to reduce surface tension and increase spreading into a submonolayer film. The pristine PCT-NBr films display bundled and aggregated structures. The bundles are likely formed from multiple single micelles, and the film as a whole retains a homogeneous fibrous morphology (Figure S16a). With $FeBr_3$ or $FeCl_3$ doping, the fiber diameters become less uniform, and overall disorder increases (Figure S16b, c), but the basic fibral morphology is retained. This result is consistent with SAXS observations, which indicate that doping with $FeCl_3$ induces some structural disorder in the polymer micelles. Based on the AFM results, the disorder appears to be similar for the $FeCl_3$- and $FeBr_3$-doped samples. Top-view AFM images of bulk films used for spectroscopic and conductivity measurements were also collected (Figure S17a, b). Although less resolved than the submonolayer films, both pristine and doped PCT-NBr exhibit a fibrous morphology and similar film roughness. Notably, although both AFM and solution-phase SAXS reveal disorder at the 10s to 100s of nanometers level, the local ordering in $FeCl_3$- and $FeBr_3$-doped PCT-NBr films remains largely preserved, as evidenced by the fact that bandgap absorption, which is highly sensitive to polymer chain formation, remains unchanged in both peak position and vibrionic structure upon doping (Figures 7 and S18).

Finally, in considering possible applications of these water-processable polymers, we consider the ionic conductivity. Due to their intrinsic ionic nature, CPEs typically exhibit high ionic conductivity. This property was evaluated for PCT-NBr films exposed to organic electrolytes by using electrochemical impedance spectroscopy (EIS). Electronic and ionic conductivities were determined using a switchable combination of a three-electrode and a two-electrode configuration, so that the film could be effectively doped electrochemically and the electronic and ionic conductivity values could be separated. See the Experimental section for details on the method used.[93] Upon electrochemical doping, both electronic and ionic conductivities increased due to the injection of charge carriers,

https://doi.org/10.1021/acsami.5c24820
ACS Appl. Mater. Interfaces 2026, 18, 11795−11808

with ionic conductivity reaching 2.8 × 10^{-5} S·cm^{-1} (Figure S19). These results demonstrate that micelle-forming PCT-NBr supports efficient charge transport, enabled by its ionic structure and porous fibrous morphology.

Further investigation is needed to understand the details of polymer structure in the doped film, and that is the focus of an ongoing study. Nonetheless, these preliminary conductivity and morphology measurements highlight the potential of micelle-forming CPEs for the fabrication of conductive films through single-step aqueous processing.

CONCLUSION

This study demonstrated that the CPE poly(cyclopentadithiophene-*alt*-thiophene) (PCT-NBr), which self-assembles into cylindrical micelles in water, can be chemically doped in an aqueous solution using Fe(III)-halide oxidants. To understand how halide identity influences both micellar morphology and electronic properties, we first examined the behavior of undoped PCT-NBr in the presence of nonoxidizing salts. SAXS measurements indicated that Br^- ions, which more closely match the hydration character of the polymer's quaternary ammonium side chains, promote ion pairing, which reduces headgroup repulsion and thus straightens micellar structures by allowing for more polymer chains per micelle. In contrast, ion exchange of the polymer's Br^- ions with Cl^- ions led to reduced ion pairing. This is accompanied by a decrease in micelle diameter that we associate with a reduction in the number of polymer chains per micelle and an accompanying increase in the ability of the thinner cylindrical micelles to bend. Electronically, the favorability of side-chain interactions with Br^- ions is reflected in a red shift of the polymer's bandgap absorption. This spectroscopic shift reflects both the straightening of the polymer micelles and an accumulation of Br^- ions around the micelles in a way that stabilizes the excitonic state. The increase in side-chain repulsion due to Cl^- ion exchange, which causes micellar bending and reduces the number of polymer chains per micelle, also reduced *H*-type coupling between chains within the micelles, leading to an enhancement in the *J*-type spectroscopic character.

Building on these observations, we next examined how counterion identity influences the extent and nature of PCT-NBr doping with Fe(III)-halide oxidants. Both $FeCl_3$ and $FeBr_3$ dopants spectroscopically shows progressive doping with increasing dopant concentration. Though $FeCl_3$ induced higher overall doping levels than $FeBr_3$, its maximum doping efficiency was 24%, a value that decreased with increasing dopant concentration. $FeCl_3$ was observed spectroscopically to exist primarily as $FeCl_2(H_2O)_4^+$ in acid-stabilized solution, while $FeBr_3$ primarily existed as $Fe(H_2O)_6^{3+}$. The loss in oxidation power for $FeBr_3$ due to ligand exchange of the electron-withdrawing Br^- ions with water highlights the importance of considering the lability of metal complex ligands when choosing aqueous dopants. Although it is a weaker oxidant, $FeBr_3$ produces more red-shifted P1 absorption features, indicative of more delocalized polarons. This effect is attributed to weaker Coulombic binding of polarons and larger, more polarizable Br^- counterions.

The use of HCl to stabilize the $FeCl_3$ dopant was found to reduce the order of the PCT-NBr micelles due to increased headgroup repulsion, a phenomenon that resulted in increased micellar bending. Although polaron formation typically has an ordering effect in semiconducting polymers in the solid state due to the straightening of the polymer chains by polaron delocalization, the opposite was observed in this study. Doping was instead shown to increase micellar bending due to a reduction in the hydrophobic character of the polymer backbone.

Finally, we showed that conductive PCT-NBr films could be deposited directly from doped micellar solutions, with $FeBr_3$-doped samples achieving a conductivity of 1.0 S/cm. The dopant efficiency of both dopants increases at high dopant concentrations due to a change in the speciation of the Fe(III) complexes in solution as the film dries. $FeCl_3$-doped films did not show measurable conductivity, which we associate with polaron trapping by the small, hard Cl^- counterion. Although solution-phase SAXS and AFM indicate bending in the macroscopic micelle structure upon doping in solution and in films, the invariance of the absorption spectra upon doping indicates that the local backbone structure within the micelle cores remains preserved. Additionally, the stability of this electrical conductivity under ambient conditions, combined with the high ionic conductivity of micellar films, highlights the promise of micelle-forming CPEs for environmentally friendly, single-step fabrication of conductive semiconducting polymer films.

EXPERIMENTAL SECTION

Materials

Poly(3-hexylthiophene) (P3HT, 97% regioregular) was purchased from Ossila, and 93% regioregular P3HT was purchased from Reike Metals. All other chemical reagents were obtained from commercial sources and used without further purification. Aqueous solutions were prepared by dissolving polymeric material and iron salts in Milli-Q ultrapure water. The PCT-NBr polymer was synthesized as described previously, with M_n = 30,000, M_w = 37,000, and PDI = 1.2.[19]

Characterization

Spectroscopy Measurements. UV-visible-NIR absorption spectra were recorded by using a JASCO V-770 spectrophotometer. Polymer solutions were measured using our fabricated sapphire-windowed ultrathin solution cell at a concentration of 2 mg/mL PCT-NBr unless otherwise stated.

FTIR absorption spectra were recorded for films cast on sapphire substrates using an Agilent Technologies Cary 600 Series FTIR spectrometer.

Solution SAXS. Solution-phase small-angle X-ray scattering (SAXS) data were collected at the Stanford Synchrotron Radiation Lightsource (SSRL) using beamline 4–2, and at the Advanced Light Source (ALS) at Lawrence Berkeley National Laboratory using High Throughput SAXS Beamline 12.3.1 (the SIBYLS Beamline). The samples were dissolved in Milli-Q ultrapure water at a concentration of 2 mg/mL, unless otherwise stated, loaded into a quartz capillary, and maintained at room temperature. Scattering X-rays with an energy of 12 keV were collected by using a 2D detector positioned at a sample-to-detector distance of 1.7 m. The 2D patterns were radially averaged to obtain 1D scattering curves. The SAXS data were processed using BioXTAS RAW software.[94−96] Pair distance distribution function (PDDF) plots were generated using the Bayesian Indirect Fourier Transform (BIFT) program, and bead models were constructed using the ATSAS software suite (GNOM, DAMMIF, DAMAVER) developed by the European Molecular Biology Laboratory (EMBL).[56−59,96] Global Guinier−Porod fitting was carried out in IgorPro using the Nika and Irena package.[97]

Solution Conductivity Measurement. A 1.0 M HCl solution was gradually added to different concentrations of $FeCl_3$, and the solution conductivity was tracked using an Apera Instruments PC60 Multiparameter Tester.

Ultrafiltration. Solution samples of 0.2 mg/mL PCT-NBr, doped with different concentrations of $FeCl_3$ (stabilized with HCl), were put into MilliporeSigma Amicon Ultra-4 centrifugal filter units with a 3 kDa regenerated cellulose filter. The filter units were centrifuged at 4400 rpm in an Eppendorf Centrifuge 5702 until approximately half the volume of the solutions passed through the filter.

Fe Content Colorimetric Analysis. The Bipyridyl Reducing Buffer solution (Bipy-Red Buffer) was made with 24 mM H_2SO_4, 2.5 mg/mL hydroxylamine hydrochloride, 0.25 mg/mL 2,2′-bipyridine, and 10 mg/mL sodium acetate. The Bipyridyl Buffer solution (Bipy Buffer) was made with 24 mM H_2SO_4, 0.25 mg/mL 2,2′-bipyridine, and 10 mg/mL sodium acetate. Filtrates and buffer solutions (Bipy-Red Buffer or Bipy Buffer) were mixed in a 1:4 volumetric ratio for spectroscopic analysis. To determine the total iron content, all iron species in the filtrate were chemically reduced to Fe(II) using hydroxylamine hydrochloride in a Bipy-Red Buffer solution. The resulting Fe(II)-bipy complex was then quantified by measuring the absorbance at 522 nm using a pre-established calibration curve (Figure S7). Separately, the Fe(II) content was measured directly by mixing the filtrate with Bipy Buffer. The relative concentrations of Fe(II) and Fe(III) species in the filtrate were deconvoluted using full-spectrum multivariate fitting (Figure S8).

Film Preparation. PCT-NBr (10 mg/mL) was dissolved in Milli-Q ultrapure water with varying concentrations of dopants. The resulting solutions were drop-cast onto precleaned substrates (glass, sapphire, indium tin oxide [ITO], or interdigitated microelectrodes [IDMs]) and spun at 1500 rpm for 60 s, followed by spinning at 2500 rpm for another 30 s to remove any remaining solvent and dry the film. The as-spun films were used for further characterization without additional processing.

All P3HT films (both 97% regioregular and 93% regioregular) were cast using 20 mg/mL solutions from *o*-dichlorobenzene (*o*-DCB). The polymer solutions were stirred until fully dissolved (~8 h) with constant stirring (300 rpm). The 2% P3HT solutions were spin-coated onto the substrates at 1000 rpm for 60 s, followed by 4000 rpm for 5 s. The polymer films were left in the nitrogen glovebox overnight to fully dry. For doping, the pristine P3HT polymer films were exposed to a dopant solution for a duration of 80 s before spinning at 4000 rpm for 10 s to remove any residual dopant solution. Doping solutions were made by mixing varying amounts of F_4TCNQ with a fixed volume of lithium bis(trifluoromethanesulfonyl)imide (LiTFSI) stock solution (209 mM) in *n*-butylacetate (*n*-BA), yielding the F_4TCNQ concentrations reported in the legends, while the LiTFSI concentration remained constant at 104 mM.

Cyclic Voltammetry (CV). CV plots were recorded by using a BioLogic VSP Potentiostat. For the CV of $FeCl_3$ and $FeBr_3$ aqueous solutions, a glassy carbon electrode was used as the working electrode, platinum (Pt) as the counter electrode, and Ag/AgCl as the reference electrode, with a sweep rate of 10 mV/s. For ferrocene, a glassy carbon electrode was used as the working electrode, Pt as the counter electrode, silver wire (Ag) as a pseudoreference electrode, and 1 M $NaClO_4$ in acetonitrile as the electrolyte, with a sweep rate of 50 mV/s. The CV of PCT-NBr films spin-cast on ITO was recorded using Pt as the counter electrode and Ag as a pseudoreference electrode, with 1 M $NaClO_4$ in acetonitrile as the electrolyte with a sweep rate of 10 mV/s. All data shown were collected on the second CV scan.

Conductivity Measurements. Conductivity values were obtained from sheet resistance and thickness measurements on 1.2 × 1.2 cm glass substrates following film fabrication and electrode deposition. Gold electrodes (45 nm thick) were evaporated on the doped films using the Angstrom Engineering Nexdep thermal evaporator at a pressure lower than 1×10^{-6} Torr and a deposition rate of 0.5 $Å \cdot s^{-1}$. Sheet resistance values were determined using the van der Pauw technique[98] with a Lakeshore MeasureReady M91 FastHall instrument (source current of 10 μA). Carrier densities were probed using Hall effect measurements performed at a source current of 10 μA and a fixed magnetic field of 1.023 T. Thickness values were obtained from profilometry by using a Dektak 150 stylus profilometer.

Atomic Force Microscopy (AFM). Freshly cleaved mica substrates were prepared by using adhesive tape. PCT-NBr was dissolved in Milli-Q ultrapure water and mixed with $FeCl_3$/HCl or $FeBr_3$/HBr to obtain a polymer concentration of 50 μg/mL, an acid concentration of 0.025 mM, and an Fe(III) dopant concentration of 0.3 mM. The solutions were drop-cast onto the freshly cleaved mica and dried under ambient conditions. AFM measurements were performed on a Bruker Dimension FastScan SPM instrument using a ScanAsyst-Air-HPI probe in PeakForce Tapping mode. Height sensor images were processed and analyzed to obtain topographical profiles.

Electrochemical Impedance Spectroscopy (EIS). Interdigitated microelectrodes (Metrohm DropSens DRP-G-IDEAU5-U20) were rinsed with isopropyl alcohol and dried prior to film deposition. Each device consists of two interdigitated gold electrodes with two connection tracks on a glass substrate (22.8 × 7.6 × 0.7 mm). The microelectrode array contains 250 pairs of digits, each with a length of 6760 μm, a width of 3 μm, a height of 200 nm, and a 5 μm gap between digits. Impedance measurements were performed using a BioLogic VSP potentiostat with Pt as the counter electrode, Ag as a pseudoreference electrode, and 1 M $NaClO_4$ in acetonitrile as the electrolyte. For electrochemical doping, the working electrode potential was held for 300 s. Ionic conductivity was measured in a three-electrode configuration by recording impedance as a function of frequency (100 kHz to 100 mHz) with a sinusoidal excitation of ±10 mV (peak-to-peak) at each doping level. Electronic conductivity was determined between the two gold IDM terminals under open-circuit conditions using the same frequency and excitation range.

■ ASSOCIATED CONTENT

Supporting Information

The Supporting Information is available free of charge at https://pubs.acs.org/doi/10.1021/acsami.5c24820.

> Additional spectroscopic data, additional CV data, additional SAXS data, and additional details on data fitting (PDF)

■ AUTHOR INFORMATION

Corresponding Authors

Sarah H. Tolbert − *Department of Chemistry and Biochemistry, University of California Los Angeles, Los Angeles, California 90095-1569, United States; Department of Materials Science and Engineering, University of California Los Angeles, Los Angeles, California 90095-1595, United States; The California NanoSystems Institute, University of California Los Angeles, Los Angeles, California 90095, United States;* orcid.org/0000-0001-9969-1582; Email: tolbert@chem.ucla.edu

Benjamin J. Schwartz − *Department of Chemistry and Biochemistry, University of California Los Angeles, Los Angeles, California 90095-1569, United States;* orcid.org/0000-0003-3257-9152; Email: schwartz@chem.ucla.edu

Yves Rubin − *Department of Chemistry and Biochemistry, University of California Los Angeles, Los Angeles, California 90095-1569, United States;* orcid.org/0000-0003-0187-9689; Email: rubin@chem.ucla.edu

Authors

Xinyu Liu − *Department of Chemistry and Biochemistry, University of California Los Angeles, Los Angeles, California 90095-1569, United States;* orcid.org/0000-0003-4978-9893

Alexander F. Simafranca − *Department of Chemistry and Biochemistry, University of California Los Angeles, Los Angeles, California 90095-1569, United States;* orcid.org/0000-0002-5274-4066

Julia Chang − *Department of Chemistry and Biochemistry, University of California Los Angeles, Los Angeles, California*

90095-1569, United States; orcid.org/0009-0004-0568-3960

Diego Garcia Vidales − *Department of Chemistry and Biochemistry, University of California Los Angeles, Los Angeles, California 90095-1569, United States*

Kara Lo − *Department of Chemistry and Biochemistry, University of California Los Angeles, Los Angeles, California 90095-1569, United States*

Yutong Wu − *Department of Chemistry and Biochemistry, University of California Los Angeles, Los Angeles, California 90095-1569, United States*

Complete contact information is available at: https://pubs.acs.org/10.1021/acsami.5c24820

Author Contributions

#X.L. and A.F.S. contributed equally to this work. The manuscript was written through the contributions of all authors. All authors have given approval to the final version of the manuscript.

Funding

This work was supported by the National Science Foundation under grant numbers CHE-2305152 and DMR-2513790.

Notes

The authors declare no competing financial interest.

ACKNOWLEDGMENTS

This work was supported by the National Science Foundation under grants CHE-2305152 and DMR-2513790. Data presented in this work made use of facilities at beamline 4-2 at the Stanford Synchrotron Radiation Lightsource and at the SIBYLS Beamline at the Advanced Photon Source. Use of the Stanford Synchrotron Radiation Lightsource, SLAC National Accelerator Laboratory, is supported by the U.S. Department of Energy, Office of Science, Office of Basic Energy Sciences under Contract No. DE-AC02-76SF00515. The SSRL Structural Molecular Biology Program is supported by the DOE Office of Biological and Environmental Research and by the National Institutes of Health, National Institute of General Medical Sciences (P30GM133894). The contents of this publication are solely the responsibility of the authors and do not necessarily represent the official views of NIGMS or NIH. The authors thank Dr. Thomas Weiss for help with beamline setup. This manuscript also contains work that was conducted at the Advanced Light Source (ALS), a national user facility operated by Lawrence Berkeley National Laboratory on behalf of the Department of Energy, Office of Basic Energy Sciences under Contract No. DE-AC02-05CH11231. Data were collected at beamline 12.3.1 through the Integrated Diffraction Analysis Technologies (IDAT) program, which is supported by the DOE Office of Biological and Environmental Research. Additional support comes from the National Institute of Health project ALS-ENABLE (P30 GM124169) and a High-End Instrumentation Grant S10OD018483. The authors thank Dr. Greg Hura for help with remote data collection.

REFERENCES

(1) Lungenschmied, C.; Dennler, G.; Neugebauer, H.; Sariciftci, S. N.; Glatthaar, M.; Meyer, T.; Meyer, A. Flexible, Long-Lived, Large-Area, Organic Solar Cells. *Solar Energy Mater. Solar Cells* **2007**, *91* (5), 379−384.

(2) Brabec, C. J.; Padinger, F.; Hummelen, J. C.; Janssen, R. A. J.; Sariciftci, N. S. Realization of Large Area Flexible Fullerene—Conjugated Polymer Photocells: A Route to Plastic Solar Cells. *Synth. Met.* **1999**, *102* (1−3), 861−864.

(3) Forrest, S. R. The Path to Ubiquitous and Low-Cost Organic Electronic Appliances on Plastic. *Nature* **2004**, *428* (6986), 911−918.

(4) Shirakawa, H.; Louis, E. J.; MacDiarmid, A. G.; Chiang, C. K.; Heeger, A. J. Synthesis of Electrically Conducting Organic Polymers: Halogen Derivatives of Polyacetylene, $(CH)_x$. *J. Chem. Soc., Chem. Commun.* **1977**, *16*, 578.

(5) Chiang, C. K.; Druy, M. A.; Gau, S. C.; Heeger, A. J.; Louis, E. J.; MacDiarmid, A. G.; Park, Y. W.; Shirakawa, H. Synthesis of Highly Conducting Films of Derivatives of Polyacetylene, (CH)x. *J. Am. Chem. Soc.* **1978**, *100* (3), 1013−1015.

(6) Steinberger, S.; Mishra, A.; Reinold, E.; Mena-Osteritz, E.; Müller, H.; Uhrich, C.; Pfeiffer, M.; Bäuerle, P. Synthesis and Characterizations of Red/Near-IR Absorbing A−D−A−D−A-Type Oligothiophenes Containing Thienothiadiazole and Thienopyrazine Central Units. *J. Mater. Chem.* **2012**, *22* (6), 2701−2712.

(7) Chen, C.-H.; Hsieh, C.-H.; Dubosc, M.; Cheng, Y.-J.; Hsu, C.-S. Synthesis and Characterization of Bridged Bithiophene-Based Conjugated Polymers for Photovoltaic Applications: Acceptor Strength and Ternary Blends. *Macromolecules* **2010**, *43* (2), 697−708.

(8) Planells, M.; Schroeder, B. C.; McCulloch, I. Effect of Chalcogen Atom Substitution on the Optoelectronic Properties in Cyclopentadithiophene Polymers. *Macromolecules* **2014**, *47* (17), 5889−5894.

(9) Bao, Z.; Rogers, J. A.; Katz, H. E. Printable Organic and Polymeric Semiconducting Materials and Devices. *J. Mater. Chem.* **1999**, *9* (9), 1895−1904.

(10) Sirringhaus, H.; Kawase, T.; Friend, R. H.; Shimoda, T.; Inbasekaran, M.; Wu, W.; Woo, E. P. High-Resolution Inkjet Printing of All-Polymer Transistor Circuits. *Science* **2000**, *290* (5499), 2123−2126.

(11) Bao, Z.; Feng, Y.; Dodabalapur, A.; Raju, V. R.; Lovinger, A. J. High-Performance Plastic Transistors Fabricated by Printing Techniques. *Chem. Mater.* **1997**, *9* (6), 1299−1301.

(12) Lee, W.; Seo, J. H.; Woo, H. Y. Conjugated Polyelectrolytes: A New Class of Semiconducting Material for Organic Electronic Devices. *Polymer* **2013**, *54* (19), 5104−5121.

(13) Jiang, H.; Taranekar, P.; Reynolds, J. R.; Schanze, K. S. Conjugated Polyelectrolytes: Synthesis, Photophysics, and Applications. *Angew. Chem., Int. Ed.* **2009**, *48* (24), 4300−4316.

(14) Gutacker, A.; Adamczyk, S.; Helfer, A.; Garner, L. E.; Evans, R. C.; Fonseca, S. M.; Knaapila, M.; Bazan, G. C.; Burrows, H. D.; Scherf, U. All-Conjugated Polyelectrolyte Block Copolymers. *J. Mater. Chem.* **2010**, *20* (8), 1423−1430.

(15) Llanes, L. C.; Lill, A. T.; Wan, Y.; Chae, S.; Yi, A.; Nguyen-Dang, T.; Kim, H. J.; Sepunaru, L.; Read de Alaniz, J.; Lu, G.; Bazan, G. C.; Nguyen, T.-Q. Side-Chain Engineering of Self-Doped Conjugated Polyelectrolytes for Organic Electrochemical Transistors. *J. Mater. Chem. C* **2023**, *11* (24), 8274−8283.

(16) Huber, R. C.; Ferreira, A. S.; Aguirre, J. C.; Kilbride, D.; Toso, D. B.; Mayoral, K.; Zhou, Z. H.; Kopidakis, N.; Rubin, Y.; Schwartz, B. J.; Mason, T. G.; Tolbert, S. H. Structure and Conductivity of Semiconducting Polymer Hydrogels. *J. Phys. Chem. B* **2016**, *120* (26), 6215−6224.

(17) Clark, A. P.-Z.; Shi, C.; Ng, B. C.; Wilking, J. N.; Ayzner, A. L.; Stieg, A. Z.; Schwartz, B. J.; Mason, T. G.; Rubin, Y.; Tolbert, S. H. Self-Assembling Semiconducting Polymers—Rods and Gels from Electronic Materials. *ACS Nano* **2013**, *7* (2), 962−977.

(18) Huber, R. C.; Ferreira, A. S.; Thompson, R.; Kilbride, D.; Knutson, N. S.; Devi, L. S.; Toso, D. B.; Challa, J. R.; Zhou, Z. H.; Rubin, Y.; Schwartz, B. J.; Tolbert, S. H. Long-Lived Photoinduced Polaron Formation in Conjugated Polyelectrolyte-Fullerene Assemblies. *Science* **2015**, *348* (6241), 1340−1343.

(19) Winchell, K. J.; Yee, P. Y.; Li, Y. L.; Simafranca, A. F.; Chang, J.; Beren, C.; Liu, X.; Garcia Vidales, D.; Thompson, R. J.; Salamat, C. Z.; Duong, Q. M.; Jordan, R. S.; Schwartz, B. J.; Gelbart, W. M.; Rubin, Y.; Tolbert, S. H. Designing Amphiphilic Conjugated

Polyelectrolytes for Self-Assembly into Straight-Chain Rod-like Micelles. *Macromolecules* **2023**, *56* (8), 3160−3170.

(20) Israelachvili, J. N. *Intermolecular and Surface Forces*; Academic Press, 2011.

(21) Collins, K. D. Charge Density-Dependent Strength of Hydration and Biological Structure. *Biophys. J.* **1997**, *72* (1), 65−76.

(22) Collins, K. D. Sticky Ions in Biological Systems. *Proc. Natl. Acad. Sci. U.S.A.* **1995**, *92* (12), 5553−5557.

(23) Collins, K. D.; Washabaugh, M. W. The Hofmeister Effect and the Behavior of Water at Interfaces. *Q. Rev. Biophys.* **1985**, *18* (4), 323−422.

(24) Washabaugh, M. W.; Collins, K. D. The Systematic Characterization by Aqueous Column Chromatography of Solutes Which Affect Protein Stability. *J. Biol. Chem.* **1986**, *261* (27), 12477−12485.

(25) He, Z.; Xie, W. J.; Liu, Z.; Liu, G.; Wang, Z.; Gao, Y. Q.; Wang, J. Tuning Ice Nucleation with Counterions on Polyelectrolyte Brush Surfaces. *Sci. Adv.* **2016**, *2* (6), No. e1600345.

(26) Gregory, S. A.; Hanus, R.; Atassi, A.; Rinehart, J. M.; Wooding, J. P.; Menon, A. K.; Losego, M. D.; Snyder, G. J.; Yee, S. K. Quantifying Charge Carrier Localization in Chemically Doped Semiconducting Polymers. *Nat. Mater.* **2021**, *20* (10), 1414−1421.

(27) Baustert, K. N.; Abtahi, A.; Ayyash, A. N.; Graham, K. R. Impact of the Anion on Electrochemically Doped Regioregular and Regiorandom Poly(3-hexylthiophene). *J. Polym. Sci.* **2022**, *60* (3), 602−609.

(28) Stanfield, D. A.; Wu, Y.; Tolbert, S. H.; Schwartz, B. J. Controlling the Formation of Charge Transfer Complexes in Chemically Doped Semiconducting Polymers. *Chem. Mater.* **2021**, *33* (7), 2343−2356.

(29) Stanfield, D. A.; Mehmedović, Z.; Schwartz, B. J. Vibrational Stark Effect Mapping of Polaron Delocalization in Chemically Doped Conjugated Polymers. *Chem. Mater.* **2021**, *33* (21), 8489−8500.

(30) Tsokkou, D.; Cavassin, P.; Rebetez, G.; Banerji, N. Bipolarons Rule the Short-Range Terahertz Conductivity in Electrochemically Doped P3HT. *Mater. Horiz.* **2022**, *9* (1), 482−491.

(31) Jacobs, I. E.; Aasen, E. W.; Oliveira, J. L.; Fonseca, T. N.; Roehling, J. D.; Li, J.; Zhang, G.; Augustine, M. P.; Mascal, M.; Moule, A. J. Comparison of Solution-Mixed and Sequentially Processed P3HT: F4TCNQ Films: Effect of Doping-Induced Aggregation on Film Morphology. *J. Mater. Chem. C* **2016**, *4* (16), 3454−3466.

(32) Scholes, D. T.; Hawks, S. A.; Yee, P. Y.; Wu, H.; Lindemuth, J. R.; Tolbert, S. H.; Schwartz, B. J. Overcoming Film Quality Issues for Conjugated Polymers Doped with F4TCNQ by Solution Sequential Processing: Hall Effect, Structural, and Optical Measurements. *J. Phys. Chem. Lett.* **2015**, *6* (23), 4786−4793.

(33) Patel, S. N.; Glaudell, A. M.; Kiefer, D.; Chabinyc, M. L. Increasing the Thermoelectric Power Factor of a Semiconducting Polymer by Doping from the Vapor Phase. *ACS Macro Lett.* **2016**, *5* (3), 268−272.

(34) Hynynen, J.; Kiefer, D.; Yu, L.; Kroon, R.; Munir, R.; Amassian, A.; Kemerink, M.; Müller, C. Enhanced Electrical Conductivity of Molecularly p-Doped Poly(3-Hexylthiophene) through Understanding the Correlation with Solid-State Order. *Macromolecules* **2017**, *50* (20), 8140−8148.

(35) Lim, E.; Peterson, K. A.; Su, G. M.; Chabinyc, M. L. Thermoelectric Properties of Poly(3-Hexylthiophene) (P3HT) Doped with 2,3,5,6-Tetrafluoro-7,7,8,8-Tetracyanoquinodimethane (F4TCNQ) by Vapor-Phase Infiltration. *Chem. Mater.* **2018**, *30* (3), 998−1010.

(36) Kang, K.; Watanabe, S.; Broch, K.; Sepe, A.; Brown, A.; Nasrallah, I.; Nikolka, M.; Fei, Z.; Heeney, M.; Matsumoto, D.; Marumoto, K.; Tanaka, H.; Kuroda, S.; Sirringhaus, H. 2D Coherent Charge Transport in Highly Ordered Conducting Polymers Doped by Solid-State Diffusion. *Nat. Mater.* **2016**, *15* (8), 896−902.

(37) Hamidi-Sakr, A.; Biniek, L.; Bantignies, J.-L.; Maurin, D.; Herrmann, L.; Leclerc, N.; Lévêque, P.; Vijayakumar, V.; Zimmermann, N.; Brinkmann, M. A Versatile Method to Fabricate Highly In-Plane Aligned Conducting Polymer Films with Anisotropic Charge Transport and Thermoelectric Properties: The Key Role of Alkyl Side Chain Layers on the Doping Mechanism. *Adv. Funct. Mater.* **2017**, *27* (25), 1700173.

(38) Vijayakumar, V.; Zaborova, E.; Biniek, L.; Zeng, H.; Herrmann, L.; Carvalho, A.; Boyron, O.; Leclerc, N.; Brinkmann, M. Effect of Alkyl Side Chain Length on Doping Kinetics, Thermopower, and Charge Transport Properties in Highly Oriented F4TCNQ-Doped PBTTT Films. *ACS Appl. Mater. Interfaces* **2019**, *11* (5), 4942−4953.

(39) Hawks, S. A.; Aguirre, J. C.; Schelhas, L. T.; Thompson, R. J.; Huber, R. C.; Ferreira, A. S.; Zhang, G.; Herzing, A. A.; Tolbert, S. H.; Schwartz, B. J. Comparing Matched Polymer: Fullerene Solar Cells Made by Solution-Sequential Processing and Traditional Blend Casting: Nanoscale Structure and Device Performance. *J. Phys. Chem. C* **2014**, *118* (31), 17413−17425.

(40) Lee, K. H.; Schwenn, P. E.; Smith, A. R. G.; Cavaye, H.; Shaw, P. E.; James, M.; Krueger, K. B.; Gentle, I. R.; Meredith, P.; Burn, P. L. Morphology of All-Solution-Processed "Bilayer" Organic Solar Cells. *Adv. Mater.* **2011**, *23* (6), 766−770.

(41) Wang, D. H.; Moon, J. S.; Seifter, J.; Jo, J.; Park, J. H.; Park, O. O.; Heeger, A. J. Sequential Processing: Control of Nanomorphology in Bulk Heterojunction Solar Cells. *Nano Lett.* **2011**, *11* (7), 3163−3168.

(42) Zhang, G.; Huber, R. C.; Ferreira, A. S.; Boyd, S. D.; Luscombe, C. K.; Tolbert, S. H.; Schwartz, B. J. Crystallinity Effects in Sequentially Processed and Blend-Cast Bulk-Heterojunction Polymer/Fullerene Photovoltaics. *J. Phys. Chem. C* **2014**, *118* (35), 18424−18435.

(43) Scholes, D. T.; Yee, P. Y.; McKeown, G. R.; Li, S.; Kang, H.; Lindemuth, J. R.; Xia, X.; King, S. C.; Seferos, D. S.; Tolbert, S. H.; Schwartz, B. J. Designing Conjugated Polymers for Molecular Doping: The Roles of Crystallinity, Swelling, and Conductivity in Sequentially-Doped Selenophene-Based Copolymers. *Chem. Mater.* **2019**, *31* (1), 73−82.

(44) Untilova, V.; Biskup, T.; Biniek, L.; Vijayakumar, V.; Brinkmann, M. Control of Chain Alignment and Crystallization Helps Enhance Charge Conductivities and Thermoelectric Power Factors in Sequentially Doped P3HT: F4TCNQ Films. *Macromolecules* **2020**, *53* (7), 2441−2453.

(45) Wu, E. C.; Salamat, C. Z.; León Ruiz, O.; Qu, T.; Kim, A.; Tolbert, S. H.; Schwartz, B. J. Counterion Control and the Spectral Signatures of Polarons, Coupled Polarons, and Bipolarons in Doped P3HT Films. *Adv. Funct. Mater.* **2023**, *33* (19), 2213652.

(46) Colaneri, N.; Nowak, M.; Spiegel, D.; Hotta, S.; Heeger, A. J. Bipolarons in Poly(3-Methylthiophene): Spectroscopic, Magnetic, and Electrochemical Measurements. *Phys. Rev. B* **1987**, *36* (15), 7964−7964.

(47) Voss, M. G.; Challa, J. R.; Scholes, D. T.; Yee, P. Y.; Wu, E. C.; Liu, X.; Park, S. J.; Leon Ruiz, O.; Subramaniyan, S.; Chen, M.; Jenekhe, S. A.; Wang, X.; Tolbert, S. H.; Schwartz, B. J. Driving Force and Optical Signatures of Bipolaron Formation in Chemically Doped Conjugated Polymers. *Adv. Mater.* **2021**, *33* (3), 2000228.

(48) Voss, M. G.; Scholes, D. T.; Challa, J. R.; Schwartz, B. J. Ultrafast Transient Absorption Spectroscopy of Doped P3HT Films: Distinguishing Free and Trapped Polarons. *Faraday Discuss.* **2019**, *216*, 339−362.

(49) Wu, E. C.; Schwartz, B. J. Does the Traditional Band Picture Describe the Electronic Structure of Doped Conjugated Polymers? TD-DFT and Natural Transition Orbital Study of Doped P3HT. *J. Chem. Theory Comput.* **2023**, *19* (19), 6761−6769.

(50) Ghosh, R.; Luscombe, C. K.; Hambsch, M.; Mannsfeld, S. C. B.; Salleo, A.; Spano, F. C. Anisotropic Polaron Delocalization in Conjugated Homopolymers and Donor−Acceptor Copolymers. *Chem. Mater.* **2019**, *31* (17), 7033−7045.

(51) Aubry, T. J.; Winchell, K. J.; Salamat, C. Z.; Basile, V. M.; Lindemuth, J. R.; Stauber, J. M.; Axtell, J. C.; Kubena, R. M.; Phan, M. D.; Bird, M. J.; Spokoyny, A. M.; Tolbert, S. H.; Schwartz, B. J. Tunable Dopants with Intrinsic Counterion Separation Reveal the Effects of Electron Affinity on Dopant Intercalation and Free Carrier

Production in Sequentially Doped Conjugated Polymer Films. *Adv. Funct. Mater.* **2020**, *30* (28), 2001800.

(52) Scholes, D. T.; Yee, P. Y.; Lindemuth, J. R.; Kang, H.; Onorato, J.; Ghosh, R.; Luscombe, C. K.; Spano, F. C.; Tolbert, S. H.; Schwartz, B. J. The Effects of Crystallinity on Charge Transport and the Structure of Sequentially Processed F4TCNQ-Doped Conjugated Polymer Films. *Adv. Funct. Mater.* **2017**, *27* (44), 1702654.

(53) Allec, N.; Choi, M.; Yesupriya, N.; Szychowski, B.; White, M. R.; Kann, M. G.; Garcin, E. D.; Daniel, M.-C.; Badano, A. Small-Angle X-ray Scattering Method to Characterize Molecular Interactions: Proof of Concept. *Sci. Rep.* **2015**, *5* (1), 12085.

(54) Svergun, D. I.; Koch, M. H. J. Small-Angle Scattering Studies of Biological Macromolecules in Solution. *Rep. Prog. Phys.* **2003**, *66* (10), 1735.

(55) Mertens, H. D. T.; Svergun, D. I. Structural Characterization of Proteins and Complexes Using Small-Angle X-Ray Solution Scattering. *J. Struct. Biol.* **2010**, *172* (1), 128−141.

(56) Hansen, S. Bayesian Estimation of Hyperparameters for Indirect Fourier Transformation in Small-Angle Scattering. *J. Appl. Crystallogr.* **2000**, *33* (6), 1415−1421.

(57) Volkov, V. V.; Svergun, D. I. Uniqueness of Ab-Initio Shape Determination in Small-Angle Scattering. *J. Appl. Crystallogr.* **2003**, *36* (3), 860−864.

(58) Franke, D.; Svergun, D. I. DAMMIF, a Program for Rapid Ab-Initio Shape Determination in Small-Angle Scattering. *J. Appl. Crystallogr.* **2009**, *42* (2), 342−346.

(59) Svergun, D. I. Restoring Low-Resolution Structure of Biological Macromolecules from Solution Scattering Using Simulated Annealing. *Biophys. J.* **1999**, *76* (6), 2879−2886.

(60) Cardona, C. M.; Li, W.; Kaifer, A. E.; Stockdale, D.; Bazan, G. C. Electrochemical Considerations for Determining Absolute Frontier Orbital Energy Levels of Conjugated Polymers for Solar Cell Applications. *Adv. Mater.* **2011**, *23*, 2367−2371.

(61) Tsierkezos, N. G. Cyclic Voltammetric Studies of Ferrocene in Nonaqueous Solvents in the Temperature Range from 248.15 to 298.15 K. *J. Solution Chem.* **2007**, *36* (3), 289−302.

(62) Ehtiati, K.; Moghaddam, S. Z.; Klok, H.-A.; Daugaard, A. E.; Thormann, E. Specific Counterion Effects on the Swelling Behavior of Strong Polyelectrolyte Brushes. *Macromolecules* **2022**, *55* (12), 5123−5130.

(63) Manning, G. S. Limiting Laws and Counterion Condensation in Polyelectrolyte Solutions. I. Colligative Properties. *J. Chem. Phys.* **1969**, *51* (3), 924−933.

(64) Boström, M.; Williams, D. R. M.; Ninham, B. W. The Influence of Ionic Dispersion Potentials on Counterion Condensation on Polyelectrolytes. *J. Phys. Chem. B* **2002**, *106* (32), 7908−7912.

(65) Kasha, M.; Rawls, H. R.; El-Bayoumi, M. A. The Exciton Model in Molecular Spectroscopy. *Pure Appl. Chem* **1965**, *11* (3−4), 371−392.

(66) Spano, F. C. The Spectral Signatures of Frenkel Polarons in H- and J-Aggregates. *Acc. Chem. Res.* **2010**, *43* (3), 429−439.

(67) Clark, J.; Silva, C.; Friend, R. H.; Spano, F. C. Role of Intermolecular Coupling in the Photophysics of Disordered Organic Semiconductors: Aggregate Emission in Regioregular Polythiophene. *Phys. Rev. Lett.* **2007**, *98* (20), 206406.

(68) Yamagata, H.; Maxwell, D. S.; Fan, J.; Kittilstved, K. R.; Briseno, A. L.; Barnes, M. D.; Spano, F. C. HJ-Aggregate Behavior of Crystalline 7,8,15,16-Tetraazaterrylene: Introducing a New Design Paradigm for Organic Materials. *J. Phys. Chem. C* **2014**, *118* (5), 28842−28854.

(69) Baes, C. F.; Mesmer, R. E. *The Hydrolysis of Cations*; Wiley, 1986.

(70) Jamett, N. E.; Hernández, P. C.; Casas, J. M.; Taboada, M. E. Speciation in the Fe(III)-Cl(I)-H_2O System at 298.15 K, 313.15 K, and 333.15 K (25 °C, 40 °C, and 60 °C). *Metall. Mater. Trans. B* **2018**, *49*, 451−459.

(71) Wu, B.; Zhang, G.; Zhang, L.; Song, X.; Zhang, S.; Zhu, B.-Z. Key Factors in the Ligand Effects on the Photo Redox Cycling of Aqueous Iron Species. *Geochim. Cosmochim. Acta* **2020**, *281*, 1−11.

(72) Lin, L.; Husek, J.; Biswas, S.; Baumler, S. M.; Adel, T.; Ng, K. C.; Baker, L. R.; Allen, H. C. Iron (III) Speciation Observed at Aqueous and Glycerol Surfaces: Vibrational Sum Frequency and X-Ray. *J. Am. Chem. Soc.* **2019**, *141* (34), 13525−13535.

(73) Ng, K. C.; Adel, T.; Lao, K. U.; Varmecky, M. G.; Liu, Z.; Arrad, M.; Allen, H. C. Iron (III) Chloro Complexation at the Air−Aqueous $FeCl_3$ Interface via Second Harmonic Generation Spectroscopy. *J. Phys. Chem. C* **2022**, *126* (36), 15386−15396.

(74) Baumler, S. M.; Hartt, V. W. H.; Allen, H. C. Hydration of Ferric Chloride and Nitrate in Aqueous Solutions: Water-Mediated Ion Pairing Revealed by Raman Spectroscopy. *Phys. Chem. Chem. Phys.* **2019**, *21* (35), 19172−19180.

(75) Music, S.; Krehula, S.; Popović, S. Effect of HCl Additions on Forced Hydrolysis of $FeCl_3$ Solutions. *Mater. Lett.* **2004**, *58* (21), 2640−2645.

(76) Zhan, X.; Xu, S.; Yang, M.; Shen, Y.; Wan, M. Vibration and Xray Photoelectron Spectroscopies of $FeCl_3$-Doped Poly(pdiethynylbenzene). *Eur. Polym. J.* **2002**, *38* (10), 2057−2061.

(77) Murrey, T. L.; Riley, M. A.; Gonel, G.; Antonio, D. D.; Filardi, L.; Shevchenko, N.; Mascal, M.; Moulé, A. J. Anion Exchange Doping: Tuning Equilibrium to Increase Doping Efficiency in Semiconducting Polymers. *J. Phys. Chem. Lett.* **2021**, *12* (5), 1284−1289.

(78) Liu, W.; Etschmann, B.; Brugger, J.; Spiccia, L.; Foran, G.; McInnes, B. UV−Vis Spectrophotometric and XAFS Studies of Ferric Chloride Complexes in Hyper-Saline LiCl Solutions at 25−90 °C. *Chem. Geol.* **2006**, *231* (4), 326−349.

(79) Torras, M.; Moya, C.; Pasquevich, G. A.; Roig, A. Accurate Iron Quantification in Colloids and Nanocomposites by a Simple UV-Vis Protocol. *Microchim. Acta* **2020**, *187* (9), 488.

(80) Lalwani, S. M.; Hellikson, K.; Batys, P.; Lutkenhaus, J. L. Counter Anion Type Influences the Glass Transition Temperature of Polyelectrolyte Complexes. *Macromolecules* **2024**, *57* (5), 4695−4705.

(81) Yoo, S.; Lei, Y. A.; Zeng, X. C. Effect of Polarizability of Halide Anions on the Ionic Solvation in Water Clusters. *J. Phys. Chem. A* **2003**, *119* (1), 6083−6091.

(82) Wu, Y.; Salamat, C. Z.; León Ruiz, A.; Simafranca, A. F.; Akmanşen-Kalayci, N.; Wu, E. C.; Doud, E.; Mehmedović, Z.; Lindemuth, J. R.; Phan, M. D.; Spokoyny, A. M.; Schwartz, B. J.; Tolbert, S. H. Title. *Chem. Mater.* **2024**, *36* (11), 5552−5562.

(83) Yee, P. Y.; Scholes, D. T.; Schwartz, B. J.; Tolbert, S. H. Dopant-Induced Ordering of Amorphous Regions in Regiorandom P3HT. *J. Phys. Chem. Lett.* **2019**, *10* (17), 4929−4934.

(84) Lim, E.; Glaudell, A. M.; Miller, R.; Chabinyc, M. L. The Role of Ordering on the Thermoelectric Properties of Blends of Regioregular and Regiorandom Poly(3-hexylthiophene). *Adv. Electron. Mater.* **2019**, *5* (11), 1800915.

(85) Wang, C.; Rivnay, J.; Himmelberger, S.; Vakhshouri, K.; Toney, M. F.; Gomez, E. D.; Salleo, A. Ultrathin Body Poly(3-hexylthiophene) Transistors with Improved Short-Channel Performance. *ACS Appl. Mater. Interfaces* **2013**, *5* (7), 2342−2346.

(86) Koutsoukos, P. G.; Kofina, A. N.; Kanellopoulou, D. G. Pure Appl. *Chem* **2007**, *79* (5), 825−850.

(87) Ostwald, W. *Lehrbuch der Allgemeinen Chemie*; Wilhelm Engelmann: Leipzig, 1896; Vol. *2*, pp. 848−849.

(88) Lindemuth, J.; Mizuta, S.-I. Hall Measurements on Low-Mobility Materials and High Resistivity Materials. In *Thin Film Solar Technology III*; SPIE, 2011, Vol. *8110*, pp. 65−71. .

(89) Chen, Y.; Yi, H. T.; Podzorov, V. High-Resolution AC Measurements of the Hall Effect in Organic Field-Effect Transistors. *Phys. Rev. Appl.* **2016**, *5* (3), 034008.

(90) Werner, F. Hall Measurements on Low-Mobility Thin Films. *J. Appl. Phys.* **2017**, *122* (13), 135306.

(91) Ghosh, R.; Pochas, C. M.; Spano, F. C. Polaron Delocalization in Conjugated Polymer Films. *J. Phys. Chem. C* **2016**, *120* (21), 11394−11406.

(92) Ghosh, R.; Chew, A. R.; Onorato, J.; Pakhnyuk, V.; Luscombe, C. K.; Salleo, A.; Spano, F. C. Spectral Signatures and Spatial Coherence of Bound and Unbound Polarons in P3HT Films: Theory Versus Experiment. *J. Phys. Chem. C* **2018**, *122* (31), 18048−18060.

(93) Zayat, B.; Das, P.; Thompson, B. C.; Narayan, S. R. *In Situ* Measurement of Ionic and Electronic Conductivities of Conductive Polymers as a Function of Electrochemical Doping in Battery Electrolytes. *J. Phys. Chem. C* **2021**, *125* (14), 7533−7541.

(94) Hopkins, J. B. BioXTAS RAW 2: New Developments for a Free Open-Source Program for Small-Angle Scattering Data Reduction and Analysis. *J. Appl. Crystallogr.* **2024**, *57* (1), 194−208.

(95) Hopkins, J. B.; Gillilan, R. E.; Skou, S. BioXTAS RAW: Improvements to a Free Open-Source Program for Small-Angle X-ray Scattering Data Reduction and Analysis. *J. Appl. Crystallogr.* **2017**, *50* (5), 1545−1553.

(96) Nielsen, S. S.; Toft, K. N.; Snakenborg, D.; Jeppesen, M. G.; Jacobsen, J. K.; Vestergaard, B.; Kutter, J. P.; Arleth, L. BioXTAS RAW, a Software Program for High-Throughput Automated Small-Angle X-ray Scattering Data Reduction and Preliminary Analysis. *J. Appl. Crystallogr.* **2009**, *42* (6), 959−964.

(97) Ilavsky, J.; Jemian, P. R. Irena: Tool Suite for Modeling and Analysis of Small-Angle Scattering. *J. Appl. Crystallogr.* **2009**, *42* (2), 347−353.

(98) van der Pauw, L. J. Determination of Resistivity Tensor and Hall Tensor of Anisotropic Conductors. *Philips Res. Rep.* **1961**, *16* (1), 187−199.